Properties of inductance and magnetic penetration depth in (103)-oriented $YBa_2Cu_3O_{7-\delta}$ thin films

J. Johansson,[1] K. Cedergren,[1,2] T. Bauch,[1] and F. Lombardi[1]
[1]*Department of Microtechnology and Nanoscience, Quantum Device Physics Laboratory, Chalmers University of Technology, SE-412 96 Göteborg, Sweden*
[2]*Dipartimento Scienze Fisiche, CNR-INFM Coherentia, Università di Napoli, 81031 Aversa (CE), Italy*
(Received 30 October 2008; published 12 June 2009)

We present a study of the anisotropy of the inductance in (103) $YBa_2Cu_3O_{7-\delta}$ (YBCO) films. YBCO superconducting quantum interference devices (SQUIDs) were fabricated by the biepitaxial technique. SQUIDs with (001)- and (103)-oriented YBCO electrodes characterized by different grain-boundary angles were realized on the same chip. Two extrainjection lines were attached to the (103) YBCO electrode. These devices, when operated in current injection mode, allow us to measure the inductance of the (103) YBCO electrode. We have found that the inductance L of the (103) YBCO can differ by a factor of 20 in the two extreme cases: L determined by current transport parallel to the *ab* planes and L dominated by the transport in the *c*-axis direction. The full in-plane angular dependence of the inductance has been obtained by considering geometrically identical SQUIDs oriented with different angles with respect to the [100] direction of the (103) film. From these measurements, we have determined the London penetration depths in the *ab* direction λ_{ab} and the *c* direction λ_c and their temperature dependence.

DOI: 10.1103/PhysRevB.79.214513 PACS number(s): 74.72.Bk, 74.25.Ha, 85.25.Cp, 85.25.Dq

I. INTRODUCTION

Josephson junctions (JJs) are considered the main building block for a host of exciting applications, ranging from classical electronics[1] to quantum informatics.[2] The physical properties of JJs have been well understood for conventional low critical temperature superconductors. Here, the resistively and capacitively shunted junction (RCSJ) model[3,4] well describes the dynamics of the system both in the classical and quantum limits. However, all the knowledge consolidated in the past three decades cannot be directly applied to JJs made of high critical temperature superconductors (HTS). The dynamics of HTS JJs becomes more intricate. The complex phenomenology derives both from intrinsic properties, such as the unconventional *d*-wave order parameter and anisotropic charge transport, and unavoidable structural material aspects such as faceting of the grain-boundary line.

Quite recently, experiments performed on a $YBa_2Cu_3O_{7-\delta}$ (YBCO) JJ realized by the biepitaxial technique on a (110) $SrTiO_3$ (STO) substrate have shown that the classical and quantum dynamics cannot be described by the conventional RCSJ model.[5–7] Here the grain-boundary junction is formed at the interface between the (103) YBCO film grown on the STO substrate and the (001) YBCO film obtained on a (110) CeO_2 (CeO) seed layer. For these Josephson junctions, the RCSJ model has to be extended taking into account the effect of the environment in close proximity of the grain boundary (GB).[6,8,9] In more detail, the stray capacitance C_S due to the substrate and the stray inductance L_S of the superconducting electrodes form an additional *LC* resonant circuit connected in parallel to the junction. The implementation of HTS JJs in classical and quantum electronics does require a proper understanding of the origin of these stray elements. An important example is given by superconducting quantum interference devices (SQUIDs) where an additional inductance term can strongly affect their functionality.[10] At the same time, HTS junctions have been also suggested for the realization of high performance quantum bits (two level system) taking advantage of the intrinsic properties of the *d*-wave order-parameter symmetry.[11] Under certain circumstances, the presence of an *LC* stray circuit will strongly influence the dynamics and operation of the two level system.[8,9]

In the junctions studied in Ref. 6, the stray capacitance has its origin in the large value of relative permittivity of the STO substrate. The stray inductance of the YBCO electrodes, instead, may have different origins related to the microstructure of the grain-boundary (filamentary transport[12]) intrinsic Josephson effect between *ab* planes and/or to the anisotropy of charge transport.[13] This last point is particularly important when the current transport has a significant *c*-axis component in the (103) electrode. Since YBCO has a large London penetration depth λ, in the *c*-axis direction, L_S may have a quite significant contribution coming from the kinetic term $L_k \sim \lambda^2$.[1]

Here we report measurements of the full in-plane angular dependence of the kinetic inductance contribution in biepitaxial dc-SQUIDs operated in the current injection mode, where two extracurrent injection leads are attached to one of the electrodes. With this configuration, one can get a direct measure of the inductance of the electrode connected to the injection lines and in certain conditions of the London penetration depth.

Several methods have been used to measure the magnetic penetration depth λ in YBCO. Muon spin relaxation,[14] magnetically modulated microwave absorption in thin-film samples,[15] susceptibility measurements of magnetically aligned powders,[16,17] measurements of the magnetic field patterns in single junctions,[18,19] or measurements of the optical conductivity at $T > T_c$ (Ref. 20) are some important examples. For bulk samples, the penetration depth in the *ab* plane λ_{ab} is 130–140 nm;[16,17] whereas in the *c*-axis direction,

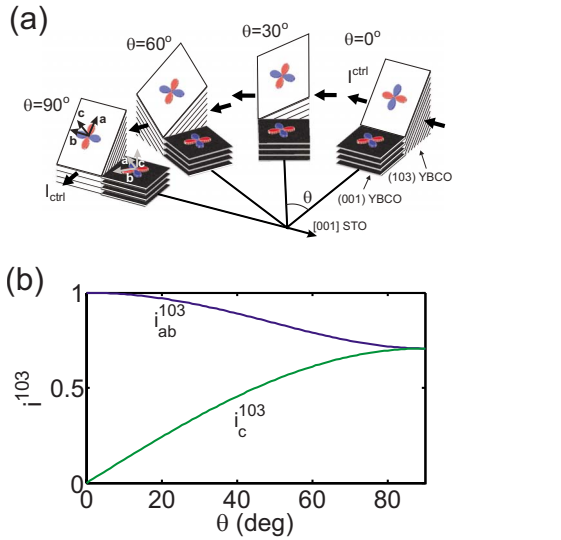

FIG. 1. (Color online) (a) Sketch of YBCO GB structure with different interface orientation. In the (001) YBCO electrode, which is grown on the CeO_2 seed layer, the CuO planes are parallel to the (110) substrate surface with a 45° rotation around the c axis. In the (103) electrode, which is grown on the (110) STO substrate, the CuO planes are slanted by 45° with respect to the substrate surface. The big arrows indicate the current path in the (103) electrode parallel to the grain boundary. (b) Normalized current components in the CuO planes i_{ab}^{103} and in the c-axis direction i_c^{103} for the charge transport parallel to the GB in the (103) electrode as a function of angle θ.

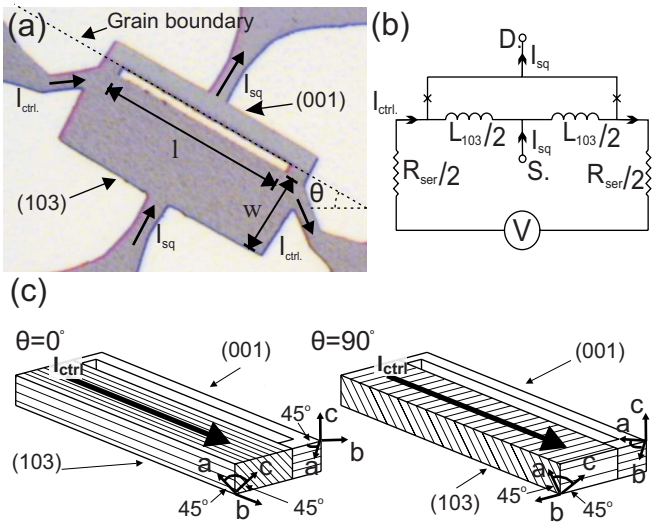

FIG. 2. (Color online) (a) Optical micrograph of a SQUID with rotation angle $\theta=30°$. The grain boundary is indicated by a dashed line. The lower part is (103)-oriented YBCO grown on (110) STO and the upper part is (001) oriented YBCO grown on a seed layer of CeO. The distance between the JJs is $l=24$ μm and the width of the (103) electrode is $w=11$ μm. (b) Schematic sketch of the measurement setup. The JJs are indicated by the crosses. (c) Schematic sketch of the orientation of the CuO planes (ab planes) in the (103) and (001) electrodes for this SQUID geometry. In the (001) electrode, the CuO planes are parallel to the substrate surface; whereas in the (103) electrode the CuO planes are slanted by 45° with respect to the substrate surface. For $\theta=0°$, the control current flows in the ab planes, while for $\theta=90°$ it has equal components in c and a directions of the (103) electrode. Depending on the current path, the kinetic inductance of the (103) electrode changes.

λ_c is 1 μm or less for optimally doped YBCO.[16,17,20] The penetration depth is highly dependent on the doping level. Values as large as 550 nm for λ_{ab} (Ref. 21) and 7.80 μm for λ_c (Ref. 20) have been reported for thin-film samples with critical temperatures of 42 and 53 K, respectively.

However, a complete study of the dependence of the London penetration depth as a function of the direction of charge transport with respect to the YBCO c axis is still missing. Our experiment initiated by the need to clarify the dynamics of HTS Josephson junctions provides a unique opportunity to investigate the anisotropic properties of HTS in a wide range of temperatures.

II. EXPERIMENTAL

The geometry of the GB structure and the orientation of the d-wave order parameter are sketched in Fig. 1. Here, θ is the angle between the grain-boundary line and the [001] in-plane direction of the STO substrate. In the (103) YBCO electrode, the charge transport parallel to the GB will have both components in the CuO planes (ab planes) and c axis direction [see Fig. 1(a)]. As a function of the angle θ, we can write for the normalized current components in the ab planes $i_{ab}^{103}=[(1/2)\sin^2\theta+\cos^2\theta)]^{1/2}$ and for the c-axis component $i_c^{103}=(1/2)^{1/2}\sin\theta$. The two current components are shown in Fig. 1(b). In the (103) YBCO electrode at $\theta=0°$, the charge transport parallel to the GB will be fully in the ab plane. For $\theta=90°$, the transport parallel to the GB will have equal components in the ab and c-axis direction of the crystal. Since the YBCO film thickness is smaller than the London penetration depth, for charge transport parallel to the GB the kinetic inductance in the (103) electrode is proportional to $L_k \sim l\lambda_{\mathrm{eff}}^2$,[1] where l is the distance between the two Josephson junctions [see Fig. 2(a)]. The effective London penetration depth λ_{eff} is defined by considering the current flow contribution in the ab planes and in the c-axis direction. This results in an expression for λ_{eff},

$$\lambda_{\mathrm{eff}}^2=\lambda_{ab}^2\cos^2\theta+\frac{1}{2}(\lambda_c^2+\lambda_{ab}^2)\sin^2\theta. \quad (1)$$

To enhance the inductance of the (103) YBCO electrode, we used a specific SQUID geometry elongated in direction parallel to the GB [see Fig. 2(a)]. The SQUID hole was kept 24×1 μm^2; the width of the JJs and the (001) electrode were 2.7 μm. The width of the (103) electrode w was 11 μm. Additionally, the (103) electrode was equipped with two current injection leads at both ends.

A set of SQUIDs with θ ranging from 0° to 90° with 10° spacing was patterned on the same chip. In Fig. 2(c), the orientation of the CuO planes in the (103) electrode is shown for $\theta=0°$ and 90°.

The samples were prepared by the biepitaxial technique described in detail in Refs. 22 and 23. Briefly, a 20-nm-thick seed layer of CeO_2 was deposited on a (110)-oriented STO

substrate, having a vicinal cut of 6°, by the pulsed laser deposition (PLD). The seed layer was patterned using the direct electron-beam (e-beam) lithography and Ar^+-ion etching through an amorphous carbon (*a* carbon) mask. The residual *a* carbon was removed by low power oxygen plasma etching and a 100-nm-thick layer of YBCO was deposited by the PLD. On the STO substrate, the YBCO grows (103) oriented and on the CeO seed-layer (001) oriented. At the boundary of the seed layer, an artificial GB is formed. Gold contact pads were made in another lithography step and finally the YBCO is patterned using the direct e-beam lithography and Ar^+-ion etching through an *a*-carbon mask. It is important to point out that the vicinal cut of the (110) STO substrate ensures a single domain (103) YBCO growth[23] and consequently a homogeneous current flow across the whole film thickness.[24] On the contrary, on exact (110) substrates because of a mixture of (103) and ($\bar{1}03$) YBCO growth, the charge transport is no longer homogeneous. In this case, the current flows in a helical manner along 90° twist boundaries between (103) and (−103) grains.[25]

All measurements were done in an Oxford Heliox VL ^{3}He refrigerator. The cryostat is magnetically shielded and located in an electromagnetically shielded environment. The switching currents of the SQUIDs were measured by ramping the current and detecting the transition from the 0 voltage state to the finite voltage state. A voltage threshold of typically 5–20 μV was used depending on the noise level.

The measurements of the (103) electrode inductance L_{103} were done by operating the SQUIDs in the direct current injection mode[26] [see Fig. 2(b)]. A known current I_{ctrl} was sent via the control lines through the (103) electrode of the SQUID while the switching currents of the device were recorded. The induced phase difference between the two junctions equals $I_{\mathrm{ctrl}}L_{103}$ (see the Appendix). The switching current of the SQUID is a 2π periodic function of the phase difference between the two JJs.[27] Thus, the electrode inductance can be extracted from the period of the switching current pattern: $L_{103}=\Phi_0/\Delta I_{\mathrm{ctrl}}$, where ΔI_{ctrl} is the period of the switching current pattern and Φ_0 is the superconducting flux quantum.[27]

Figure 3 shows the switching current pattern of two SQUIDs as a function of the control current through the (103) electrode measured at $T=280$ mK. One can clearly see the difference in periodicity ΔI_{ctrl} related to the larger component of transport along the YBCO *c* axis in the case $\theta=90°$ compared to $\theta=40°$.

The inductance values extracted from the current injection measurements are presented in Fig. 4 for various angles θ. An increase by a factor of 20 is observed between the two extreme angles $\theta=0°$ and 90°.

The total inductance of the (103) electrode can be expressed as

$$L_{103}=L_{\mathrm{geo}}+L_k=L_{\mathrm{geo}}+\mu_0\frac{l}{wt}\lambda_{\mathrm{eff}}^2, \tag{2}$$

where L_{geo} is the geometric inductance of the electrode, which is related to the magnetic flux threading the SQUID loop due to the injection current, l is the distance between the two JJs, w is the width, and t is the thickness of the (103) electrode [see Fig. 2(a)].

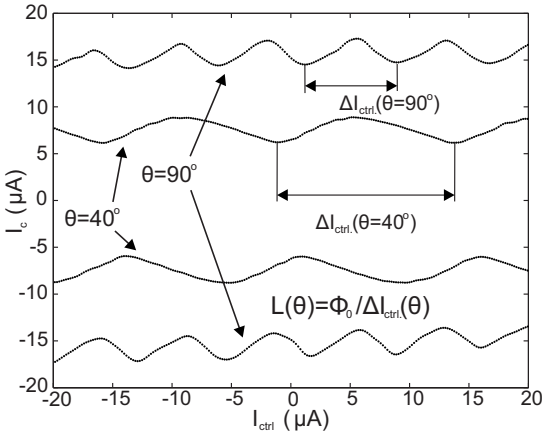

FIG. 3. Magnetic diffraction pattern as a function of control current I_{ctrl} for two SQUIDs with rotation angles $\theta=40°$ and 90° at $T=280$ mK. The inductance of the bottom electrode can be extracted from the modulation period ΔI_{ctrl}.

It is worth pointing out that Eqs. (1) and (2) are only valid for a homogeneous current flow along the length l of the (103) electrode; that is, the current flow is parallel to the GB and a homogeneous current injection along the whole width w of the electrode. For our SQUID geometry, this is a good approximation for angles $\theta>40°$. For $\theta<40°$, the current

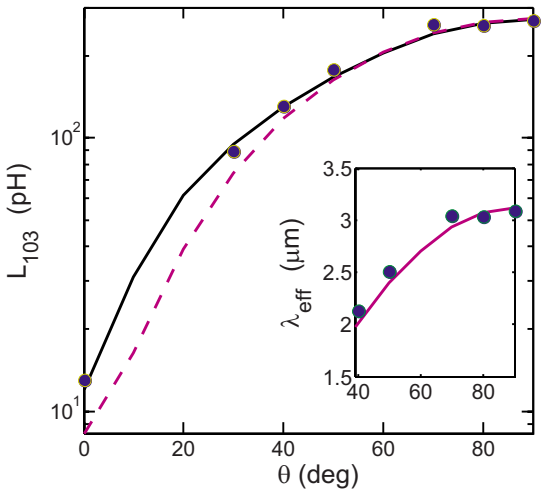

FIG. 4. (Color online) Measured inductance of the lower (103) electrode of the SQUIDs $L_{103}=L_{\mathrm{geo}}+L_k$ as a function of the angle θ at $T=280$ mK (closed circles). The measurements were done by operating the SQUIDs in current injection mode. For $\theta=0°$, $L_{103}=13$ *p*H; whereas for $\theta=90°$ the inductance increases by a factor of 20–265 *p*H. The solid line is a fit of the inductance with respect to the angle θ which is obtained by numerically calculating the current distribution in the (103) electrode. From the fit, one obtains $\lambda_{ab}=270$ nm and $\lambda_c=4.4$ μm. The dashed line is the inductance calculated from the analytical expression [Eq. (2)]. The inset shows the extracted values of the effective penetration depth λ_{eff} from the experimental data of L_{103} as a function of angle θ for $\theta\geq 40°$ (solid circles). The solid line is the analytical expression of the effective penetration depth [Eq. (1)].

coming from the injection leads will redistribute along the (103) electrode having components both parallel and perpendicular to the GB line, giving rise to corrections to the analytical expression of the inductance given by Eq. (2). Therefore, we calculated numerically the current distribution in the (103) electrode taking into account the anisotropy of the London penetration depth and the finite width of the current injection leads.[28,29] From the current distribution, we can extract both the geometric and kinetic components of the inductance. We obtain the best fit of the measured inductance values as a function of θ for $\lambda_{ab}=270$ nm and $\lambda_c=4.4$ μm, which is shown as a solid line in Fig. 4. For comparison, the inductance as a function of θ calculated from the expression given by Eq. (2) is shown as a dashed line in Fig. 4(a) using the same values for λ_{ab} and λ_c. For the geometric inductance, we used $L_{\mathrm{geo}}=6.3$ pH, which we determined from the numerical calculation of the current distribution in the (103) electrode for $\theta=0°$. One can clearly see that the analytic expression of the inductance as a function of angle θ agrees well with the numerically determined $L_{103}(\theta)$ for $\theta>40°$, while it deviates for $\theta<40°$ due to the redistribution of the injection current in the (103) electrode. With Eqs. (1) and (2), one can extract from the experimentally measured $L_{103}(\theta)$ the effective penetration depth λ_{eff} for $\theta>40°$, which is shown in the inset of Fig. 4.

The extracted values of $\lambda_{ab}=270$ nm and $\lambda_c=4.4$ μm are both larger than what is reported for optimal-doped YBCO.[16,17,20] Since the postprocessed film had a transition temperature T_c of 71 K, we believe that our results are due to the oxygen depletion. If the reduced T_c is taken into account, λ_{ab} and λ_c are in good agreement with the values reported in Ref. 30 $\lambda_{ab}=220$ nm for $T_c=70$ K and in Ref. 20 which reports $\lambda_c=3.42$ and 5.05 μm for films with T_c of 78 and 58 K, respectively.

The temperature dependence of the London penetration depth is directly correlated with the superconductive order parameter. In the past years, numerous experimental investigations have used this tool to reveal the unconventional symmetry of the order parameter in HTS. In our sample, we have the unique possibility to simultaneously measure the temperature dependence of λ_{ab} and λ_c and, in principle, to get insights into the properties of YBCO.

The (103) electrode inductance was measured with respect to temperature for three SQUIDs $\theta=0°$, 40°, and 50°. The results are presented in Fig. 5. We use the Gorter-Casimir two fluid approximation with an arbitrary exponent n to fit our data,

$$\lambda(T)=\lambda(0)\frac{1}{\sqrt{1-\left(\frac{T}{T_c}\right)^n}}. \tag{3}$$

From Eqs. (1) and (3), we derive the expression for the temperature dependence of λ_{eff} with respect to θ,

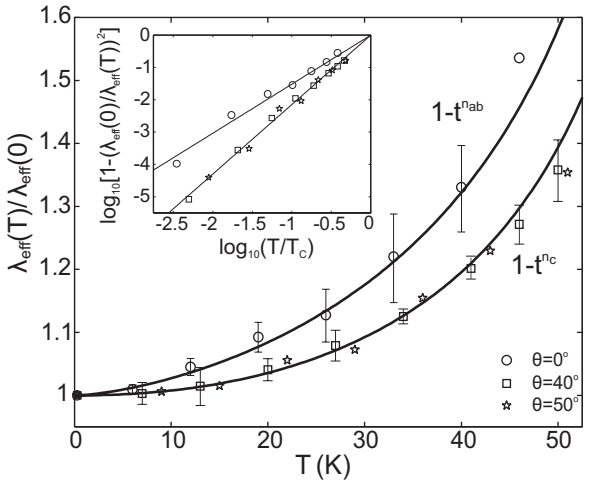

FIG. 5. Normalized temperature dependence of $\lambda_{\mathrm{eff}}(T)/\lambda_{\mathrm{eff}}(T=0)$ for $\theta=0°$, 40°, and 50°. The data (open symbols) follow the Gorter-Casimir two fluid dependence (solid line) with exponent n_c equal to 2.15 ± 0.5 for λ_c ($\theta=40°$ and 50°) and $n_{ab}=1.5\pm0.2$ for $\lambda_{ab}(\theta=0°)$ (see text for details). (Inset) $\log_{10}\{1-[\lambda_{\mathrm{eff}}(0)/\lambda_{\mathrm{eff}}(T)]^2\}$ is plotted versus $\log_{10}(T/T_c)$ for $\theta=0°$, 40°, and 50°. From the slope of the curves, the exponents n_{ab} and n_c are determined.

$$\frac{\lambda_{\mathrm{eff}}^2(\theta,0)}{\lambda_{\mathrm{eff}}^2(\theta,T)}=(1-t^{n_c})\frac{1+\frac{\lambda_{ab}^2}{\lambda_c^2}\frac{1+\cos^2\theta}{\sin^2\theta}}{1+\frac{\lambda_{ab}^2}{\lambda_c^2}\frac{1+\cos^2\theta}{\sin^2\theta}\frac{1-t^{n_c}}{1-t^{n_{ab}}}}, \tag{4}$$

where $t=T/T_c$ and n_{ab} and n_c are the exponents for the temperature dependence of the London penetration depth in ab and c directions, respectively [see Eq. (3)].

For $\theta=0°$, where the current transport in the (103) electrode is parallel to the ab planes, we get from Eqs. (1) and (3),

$$\frac{\lambda_{\mathrm{eff}}^2(\theta=0°,0)}{\lambda_{\mathrm{eff}}^2(\theta=0°,T)}=\frac{\lambda_{ab}^2(0)}{\lambda_{ab}^2(T)}=(1-t^{n_{ab}}). \tag{5}$$

For $\theta>0°$, since $\lambda_{ab}\ll\lambda_c$, we get from Eq. (4),

$$\frac{\lambda_{\mathrm{eff}}^2(\theta>0°,0)}{\lambda_{\mathrm{eff}}^2(\theta>0°,T)}\approx(1-t^{n_c}). \tag{6}$$

The temperature dependence for finite angles, where λ_{eff} is dominated by the c-axis component ($\theta=40°$ and 50°), is well described by the Gorter-Casimir approximation (6) with an exponent $n_c=2.15\pm0.05$ (see Fig. 5). This result is in good agreement with the one reported in Refs. 31 and 32 (and confirms that the temperature behavior is doping independent). λ_{ab}, which is equivalent to $\lambda_{\mathrm{eff}}(\theta=0°)$, has a much steeper temperature dependence as one can clearly see form Fig. 5. A fit with Eq. (5) yields $n_{ab}=1.5\pm0.2$. The different behavior in temperature of λ_c and λ_{ab} can be due to various origins and it is still under investigation.

III. CONCLUSION

We have measured the full in-plane angular dependence of the inductance of (103)-oriented YBCO films using dc-

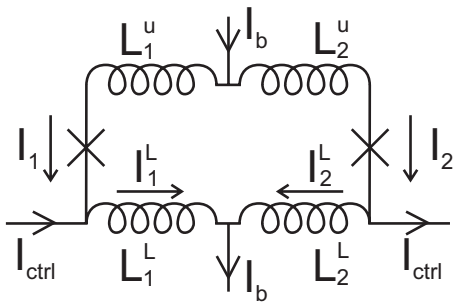

FIG. 6. Circuit diagram of a current-biased SQUID operated in the current injection mode (see text for details).

SQUIDs in current injection mode. We found that the inductance varies by a factor of 20 which is due to the large anisotropy of the London penetration depth in YBCO. From the measured inductance values, we determined $\lambda_{ab}=270$ nm and $\lambda_c=4.4$ μm. Moreover, the temperature dependence for λ_c is well described by the Gorter-Casimir approximation. The findings are of great importance for the design of electrical circuits which implement (103) YBCO films, both in the classical and quantum regimes.

ACKNOWLEDGMENTS

We would like to thank Nils Johansson for the help with the 3D sketches. This work has been partially supported by EU Nanoxide, EU STREP project MIDAS, the Swedish Research Council (VR) under the Linnaeus Center on Engineered Quantum Systems, the Swedish Research Council (VR) under the project Macroscopic quantum tunneling and coherence in superconductive *d*-wave junctions, the Knut and Alice Wallenberg Foundation, the Swedish Foundation for Strategic Research (SSF) under the project Oxide. F.L. was supported by a grant from the Knut and Alice Wallenberg Foundation.

APPENDIX

In the following, we discuss how the critical current of a current-biased SQUID operated in the current injection mode is affected by the control current. Here we consider the current-biased SQUID depicted in Fig. 6. The upper electrode contains two inductances L_1^U in the left and L_2^U in the right SQUID arm. The inductances in the left and right arms of the lower electrode are given by L_1^L and L_2^L, respectively. The dc currents across the two Josephson junctions I_1 and I_2 are given by the first Josephson relation,[27]

$$I_1 = I_{c1} \sin \varphi_1, \tag{A1}$$

$$I_2 = I_{c2} \sin \varphi_2, \tag{A2}$$

where I_{c1} and I_{c2} are the critical currents of the two Josephson junctions. φ_1 and φ_2 are the phase differences across the two junctions. According to Kirchhoff's law, we can write for the bias current

$$I_b = I_1 + I_2. \tag{A3}$$

From the fluxoid quantization around the SQUID loop, we get[1]

$$\varphi_2 - \varphi_1 = \frac{2\pi}{\Phi_0}\Phi_{\text{tot}}, \tag{A4}$$

where the total magnetic flux is given by $\Phi_{\text{tot}}=\Phi_{\text{ext}}+\Phi_{\text{self}}$. Here, Φ_{ext} is the externally applied magnetic flux and Φ_{self} is the flux generated by the currents I_1, I_2, I_1^L, and I_2^L flowing in the left and right SQUID arms, which contain both geometric and kinetic inductances (see Fig. 6). Equations (A1)–(A4) fully determine the critical current of the SQUID.[1] Moreover, from these equations, one can see that the critical current will be a Φ_0 periodic function with respect to the total magnetic flux.

The control current I_{ctrl} is injected into the left side of the lower electrode (see Fig. 6). The output of the control current is on the right side of the lower electrode. For the total magnetic flux, we can write

$$\Phi_{\text{tot}} = \Phi_{\text{ext}} + I_1 L_1^U + I_1^L L_1^L - I_2 L_2^U - I_2^L L_2^L. \tag{A5}$$

Using Kirchhoff's law, the currents flowing in the lower electrode can be expressed as follows:

$$I_1^L = I_{\text{ctrl}} + I_1, \tag{A6}$$

$$I_2^L = -I_{\text{ctrl}} + I_2. \tag{A7}$$

Inserting Eqs. (A6) and (A7) into the expression for the total magnetic flux, we get

$$\Phi_{\text{tot}} = \Phi_{\text{ext}} + I_1 L_1 - I_2 L_2 + I_{\text{ctrl}} L^L, \tag{A8}$$

where $L_1=L_1^U+L_1^L$ and $L_2=L_2^U+L_2^L$ are the inductances of the left and right SQUID arms, respectively. The inductance of the lower electrode is given by $L^L=L_1^L+L_2^L$. From Eq. (A8), we see that the term $I_{\text{ctrl}}L^L$ has the same effect as an externally applied magnetic flux Φ_{ext}. The phase difference $\varphi_2-\varphi_1$ between the two Josephson junctions [see Eq. (A4)], which is induced by the control current, is therefore solely determined by the inductance of the lower electrode L^L. Consequently, the control current periodicity ΔI_{ctrl} of the critical current of the SQUID will be given by $\Delta I_{\text{ctrl}}=\Phi_0/L^L$. Here we want to point out that the control current does split up between the upper and lower electrodes. The amount of control current flowing through the upper electrode is given by the circulating current around the SQUID loop, which is defined as $(I_2-I_1)/2$. This circulating current is induced by the term $I_{\text{ctrl}}L^L$ in Eq. (A8) for $\Phi_{\text{ext}}=0$. The same circulating current is induced in the SQUID loop when an external magnetic flux with a value $\Phi_{\text{ext}}=L^L I_{\text{ctrl}}$ is applied to the SQUID loop without injecting a control current.

[1] T. van Duzer, *Principles of Superconductive Devices and Circuits*, 2nd ed. (Prentice Hall, Upper Saddle River, NJ, 1999).
[2] Y. Makhlin, G. Schön, and A. Shnirman, Rev. Mod. Phys. **73**, 357 (2001).
[3] W. C. Stewart, Appl. Phys. Lett. **12**, 277 (1968).
[4] D. E. McCumber, J. Appl. Phys. **39**, 3113 (1968).
[5] T. Bauch, F. Lombardi, F. Tafuri, A. Barone, G. Rotoli, P. Delsing, and T. Claeson, Phys. Rev. Lett. **94**, 087003 (2005).
[6] T. Bauch, T. Lindström, F. Tafuri, G. Rotoli, P. Delsing, T. Claeson, and F. Lombardi, Science **311**, 57 (2006).
[7] F. Lombardi, T. Bauch, J. Johansson, T. Lindström, K. Cedergren, F. Tafuri, and E. Stepantsov, Physica C **435**, 8 (2006).
[8] G. Rotoli, T. Bauch, T. Lindström, D. Stornaiuolo, F. Tafuri, and F. Lombardi, Phys. Rev. B **75**, 144501 (2007).
[9] F. Lombardi, T. Bauch, G. Rotoli, T. Lindstrom, J. Johannson, K. Cedergren, F. Tafuri, and T. Claeson, IEEE Trans. Appl. Supercond. **17**, 653 (2007).
[10] D. Koelle, R. Kleiner, F. Ludwig, E. Dantsker, and J. Clarke, Rev. Mod. Phys. **71**, 631 (1999).
[11] M. H. S. Amin, A. Y. Smirnov, A. M. Zagoskin, T. Lindström, S. A. Charlebois, T. Claeson, and A. Y. Tzalenchuk, Phys. Rev. B **71**, 064516 (2005).
[12] B. H. Moeckly and R. A. Buhrman, Appl. Phys. Lett. **65**, 3126 (1994).
[13] T. Bauch, K. Cedergren, J. Johansson, G. Rotoli, F. Tafuri, and F. Lombardi, Supercond. Sci. Technol. **20**, S98 (2007).
[14] D. R. Harshman, L. F. Schneemeyer, J. V. Waszczak, G. Aeppli, R. J. Cava, B. Batlogg, L. W. Rupp, E. J. Ansaldo, and D. L. Williams, Phys. Rev. B **39**, 851 (1989).
[15] R. Karim, C. Vittoria, A. Widom, D. B. Chrisey, and J. B. Horwitz, J. Appl. Phys. **69**, 4891 (1991).
[16] A. Porch, J. R. Cooper, D. Zheng, J. Waldram, A. Campell, and P. Freeman, Physica C **214**, 350 (1993).
[17] D. N. Zheng, A. M. Campbell, J. D. Johnson, J. R. Cooper, F. J. Blunt, A. Porch, and P. A. Freeman, Phys. Rev. B **49**, 1417 (1994).
[18] O. M. Froehlich, H. Schulze, R. Gross, A. Beck, and L. Alff, Phys. Rev. B **50**, 13894 (1994).
[19] H. Sato, H. Akoh, and S. Takada, Appl. Phys. Lett. **64**, 1286 (1994).
[20] C. C. Homes, S. V. Dordevic, D. A. Bonn, R. Liang, W. N. Hardy, and T. Timusk, Phys. Rev. B **71**, 184515 (2005).
[21] J. Y. Lee, K. Paget, T. Lemberger, S. Foltyn, and X. Wu, Synth. Met. **71**, 1605 (1995).
[22] F. Lombardi, F. Tafuri, F. Ricci, F. Miletto Granozio, A. Barone, G. Testa, E. Sarnelli, J. R. Kirtley, and C. C. Tsuei, Phys. Rev. Lett. **89**, 207001 (2002).
[23] F. Miletto Granozio, U. Scotti di Uccio, F. Lombardi, F. Ricci, F. Bevilacqua, G. Ausanio, F. Carillo, and F. Tafuri, Phys. Rev. B **67**, 184506 (2003).
[24] R. P. Campion, P. J. King, K. A. Benedict, R. M. Bowley, P. S. Czerwinka, S. Misat, and S. M. Morley, Phys. Rev. B **61**, 6387 (2000).
[25] R. P. Campion, J. R. Fletcher, P. J. King, S. M. Morley, A. Polimeni, and R. G. Ormson, Supercond. Sci. Technol. **11**, 730 (1998).
[26] H. Terai, M. Hidaka, T. Satoh, and S. Tahara, Appl. Phys. Lett. **70**, 2690 (1997).
[27] M. Tinkham, *Introduction to Superconductivity*, 2nd ed. (McGraw-Hill, New York, 2004).
[28] Here we followed the approach developed by M. M. Khapaev, Jr., described in Ref. 29. We extended the approach taking into account an anisotropic London penetration depth to calculate the current distribution in the (103) electrode. The software COMSOL was used to perform the numerical finite element calculations. The detailed results of the numerical calculations will be published elsewhere.
[29] M. M. Khapaev, Jr., Supercond. Sci. Technol. **10**, 389 (1997).
[30] Y. Zuev, M. S. Kim, and T. R. Lemberger, Phys. Rev. Lett. **95**, 137002 (2005).
[31] A. Hosseini, S. Kamal, D. A. Bonn, R. Liang, and W. N. Hardy, Phys. Rev. Lett. **81**, 1298 (1998).
[32] A. Hosseini, D. M. Broun, D. E. Sheehy, T. P. Davis, M. Franz, W. N. Hardy, R. Liang, and D. A. Bonn, Phys. Rev. Lett. **93**, 107003 (2004).